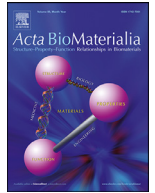




Contents lists available at ScienceDirect

Acta Biomaterialia

journal homepage: www.elsevier.com/locate/actbio

Reinforcement of bio-apatite by zinc substitution in the incisor tooth of a prawn[☆]

S. Bentov^{a,b,*}, B.A. Palmer^{c,1}, B. Bar-On^d, Y. Shelef^d, E.D. Aflalo^{a,e}, A. Sagi^{a,b,*}

^aThe National Institute for Biotechnology in the Negev (NIBN), Israel

^bThe Department of Life Sciences, Ben-Gurion University, Israel

^cThe Department of Structural Biology, Weizmann Institute of Science, Israel

^dThe Department of Mechanical Engineering, Ben-Gurion University of the Negev, Israel

^eThe Department of Life Sciences, Achva Academic College, Israel

ARTICLE INFO

Article history:

Received 8 April 2020

Revised 15 July 2020

Accepted 17 July 2020

Available online xxx

Keywords:

Biomaterialization
Zn-substituted apatite
Apatite reinforcement
Teeth-biomechanics

ABSTRACT

Various material-strengthening strategies have evolved in the cuticle and the feeding tools of arthropods. Of particular interest is the crustacean mandible, which is frequently reinforced with calcium phosphate, giving a mineralogy similar to that of human bones and teeth. We report here a biological strengthening method of apatite by Zn substitution, found in the incisor teeth of the freshwater prawn *Macrobrachium rosenbergii*. Nanoindentation measurements show a clear positive correlation between the Zn/Ca ratio and the stiffness and hardness of the composite. In the incisor, Zn-substituted apatite forms an internal vertical axis, extending from the sharp outer edges of the tooth to its basal segment. The substitution level in this zone (up to 40%) is very high compared with the levels achieved in synthetic ceramics (<20%). Finite element simulation suggests that the high-Zn axis acts as a unique internal load transfer element, directing stress from the biting cusps to the more compliant underlying layers. In light of the considerable research being invested in developing synthetic calcium phosphate derivatives for human bone and tooth grafts, the innovative mineralogy of the *M. rosenbergii* incisor may inspire beneficial biomimetic applications.

Statement of Significance

The controlled incorporation of impurities into biominerals is a widespread phenomenon in biomineralization that may pave the way to new classes of biomimetic materials. The present study reveals a biogenic mineral of zinc-substituted apatite found in the incisor teeth of a prawn. A clear correlation between zinc substitution level and stiffness and hardness, suggests that zinc substitution serves to mechanically reinforce the bioapatite. The spatial arrangement of the high-zinc apatite unveils a material-level adaptation strategy for tooth fortification, in which the rigid high-Zn structure serves as an internal load-transfer element that transmits the stress directly from the tooth's sharp cusps to the more compliant underlying layers.

© 2020 Acta Materialia Inc. Published by Elsevier Ltd. All rights reserved.

1. Introduction

The crustacean cuticle (exoskeleton) is comprised of an intricate bio-composite consisting of a chitin-protein scaffold frequently reinforced with a mineral component that dominates its mechani-

cal properties [1]. Usually the most heavily mineralized part of the exoskeleton is the mandible which is equipped with specialized tooth processes, “incisors” (for biting and cutting) and “molars” (for grinding and chewing). While calcium carbonate mineralization has been adopted by most crustaceans for overall reinforcement of the exoskeleton, in many species of the crustacean class Malacostraca (including lobsters, crayfish, prawns and shrimps) calcium phosphate, in the form of apatite and/or amorphous calcium phosphate (ACP), is deposited at specific locations in mechanically challenged sites of the mandible, which greatly improves its mechanical strength [2,3]. In these species, the mandibles display an elaborate multiphase biomineralization that combines various

[☆] Part of the Special Issue on Biomineralization: From Cells to Biomaterials, associated with the BIOMIN XV: 15th International Symposium on Biomineralization, held at the Ludwig Maximilian University, Sept 9–13, 2019, organized by Wolfgang Schmahl and Erika Griesshaber.

* Corresponding authors.

¹ Current address: Department of Chemistry, Ben-Gurion University of the Negev, Beer Sheva.

<https://doi.org/10.1016/j.actbio.2020.07.039>

1742-7061/© 2020 Acta Materialia Inc. Published by Elsevier Ltd. All rights reserved.

minerals (i.e., amorphous calcium carbonate (ACC), ACP, calcite and apatite) arranged in well-defined species-specific distribution patterns that reflect the feeding habits of the organism [2–4]. In addition to the combination of different mineral phases, the properties of the apatite can be modified by various ionic substitutions. A known characteristic of apatite mineral is the tolerance to substitutions which enable apatite to incorporate half of the elements in the periodic table within its crystal structure [5,6]. The high potential for ionic substitutions in apatite is seen in various biomineralization systems e.g. the carbonated apatite of mammalian bone or the fluorapatite of the crayfish mandible.

In the prawn, *M. rosenbergii*, the distal part of both molar and incisor teeth, is composed of calcium phosphate. The incisor is much more heavily mineralized than the molar, however not in a homogeneous manner. A vertical element, extending from the distal cusp point, down to the underlying basal layers, shows the highest mineral density. This element is the focus of this study.

2. Materials and methods

2.1. Animals

M. rosenbergii prawns were reared in artificial ponds at Ben-Gurion University of the Negev, Beer-Sheva, Israel and at the Dor Fish and Aquaculture Research Station of the Ministry of Agriculture (32.7°N, 35.0°E). The animals were anesthetized in ice-cold water before dissection. Mature teeth were extracted from specimens at an inter-molt stage and from fresh exuviae. For this study, ~200 mandibles were extracted, washed, and cleaned by immersion in NaOCl (1%) for 1 h. The mandibles stored dry at room temperature until the analyses were performed.

2.2. Sample embedding and polishing

Mandibles were embedded in Epofix™ cold-setting resin at a resin/hardener ratio (w/w) of 25:3, and then polished to reduce thickness and provide a flat surface for EDS, WDS and nanoindentation measurements. Most of the sections were longitudinal cross-sections along a proximodistal line running from the sharp edge downward, perpendicular to the incisor's distal surface.

2.3. Micro-CT

Scans were performed on a Skyscan1 1172 micro-CT machine (Skyscan). The X-ray source was set at 60 keV and 160 mA, with a resolution of 3.5 μm pixels. Specimens were scanned through 360° with 0.7° rotation increments. The projection images were reconstructed using the NRecon software (Skyscan). Volume rendering reconstructions were performed using CTvox software (Skyscan). Gray-scale images were pseudo-colored according to an RGB palette, with low mineral density in red and high density in blue.

2.4. Raman spectroscopy

Raman spectra were recorded using an inVia Raman microscope system (Renishaw plc, Gloucestershire, UK) equipped with a Leica microscope and a 785 nm, 300 mW excitation laser with a spectral range of ~200–1300 cm^{-1} . A 50 \times objective lens and 10-s exposure time were used. A 1200 grooves/mm grating gave a resolution of 2–4 cm^{-1} . Raman imaging (Renishaw plc) was performed using an inVia Qontor. Measurements were made with the Renishaw Centrus CCD detector, which allows spectral acquisitions of 1 ms and is free of ripple-effects in the near infrared region. Images were acquired using StreamLine fast imaging. The average and baseline subtraction functions of the software were used to extract

the average spectra and to detect the presence of chitin. The following measurement configurations were used: Laser wavelength, 785 nm; grating, 1200 l/mm; objective, 50 \times ; Fig. 1d, map area, 1800 μm \times 4200 μm , step size, 60 μm , number of spectra, 2200; Fig. 1e–h, map area, 852 μm \times 1761 μm and 28.4 μm , number of spectra, 1860.

2.5. Powder X-ray diffraction

Analysis was performed on milled samples of the incisors spread on a quartz plate. X-ray diffraction measurements were performed on the D8 Advance diffractometer (Bruker AXS, Karlsruhe, Germany), and a Philips model PW-1050/70 diffractometer) with a secondary graphite monochromator, two Soller slits, and a 0.2 mm receiving slit. XRD patterns within the range 3 to 75 2θ were recorded at room temperature using $\text{CuK}\alpha$ radiation ($\lambda = 1.5418 \text{ \AA}$) with the following measurement conditions: tube voltage 40 kV; tube current 40 mA; step-scan mode with a step size of 0.02° 2θ and counting time of 1 s/step. TOPAS-v.3 software (Bruker AXS, Karlsruhe, Germany, 2003). was used for structure refinement and crystallite size calculation.

2.6. Microbeam XRD

Wide angle X-ray diffraction (WAXD) measurements were obtained at the μ -Spot beamline, in the synchrotron radiation facility BESSY II, Helmholtz-Zentrum Berlin für Materialien und Energie. Polished longitudinal sections of the incisors (150 μm thick) were mounted on a y - z scanning table. The micro-beam was defined by a toroidal mirror and a pinhole of 30 μm diameter close to the sample, providing a beam size of approximately 30 μm^2 at the sample location. An energy of 15 keV ($\lambda=0.826561 \text{ \AA}$) was selected by a Mo/BC multilayer monochromator. Fluorescence spectra were collected with an energy sensitive detector (Ketek) in reflection geometry at an angle of about 45°. The K-shell fluorescence yield of calcium, normalized to the primary beam intensity, together with X-ray absorption/transmission maps were used to qualitatively map the position and orientation of the samples. The 2D WAXD patterns were obtained using a MarMosaic 225 CCD-based area detector (Rayonix) placed at a sample detector distance of 290 mm. The beam center in the detector and the sample-detector distance were calibrated using a polycrystalline quartz standard. The typical measurement time for a single frame was 30 s. Radial integration of the 2D scattering patterns was performed by using dpdak version 110. The data were normalized with respect to the primary beam monitor (ionization chamber) and corrected for background due to pinhole and air scattering.

2.7. SEM and EDS analysis

Polished tooth sections were sputter coated with platinum, gold or carbon and examined using a JEOL JSM-7400f apparatus. EDS/WDS analyses of the teeth were performed at the Institute of Earth Sciences, The Hebrew University of Jerusalem with a JEOL 8230 Superprobe EPMA with EDS detector and four wavelength-dispersive spectrometers for WDS microanalysis. Beam conditions were set to 15 keV and 15 nA. All phases were analyzed for the elements Ca, P, Zn, O, and C. The system was calibrated using mineral standards from SPI for the different elements (analytical standards AS 02,753-AB 53). EDS data was processed using a ZAF correction procedure. The location of the analyzed discrete points was chosen randomly within the area of interest (i.e. the central axis). The locations of the line profile analyses were randomly chosen, perpendicularly to the central axis of the tooth section, while the

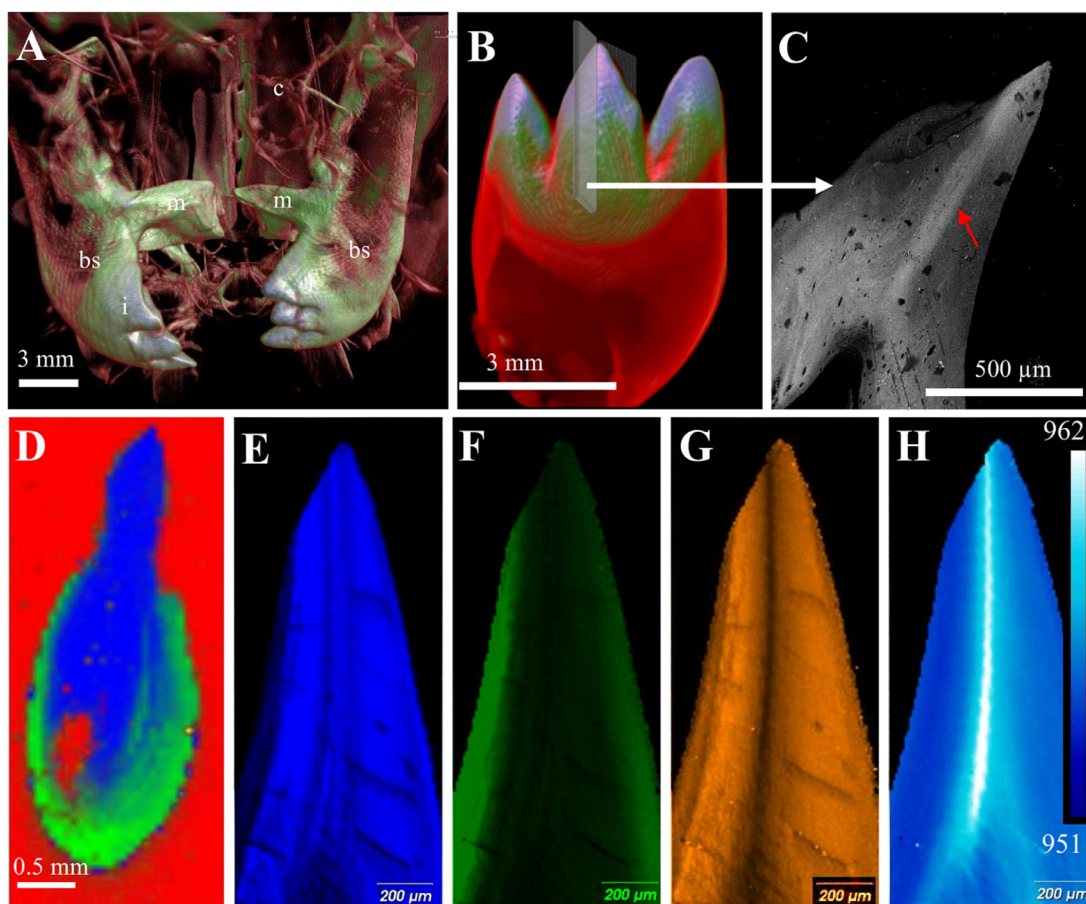


Fig. 1. General structure and mineralogy of the mandible of the prawn *M. rosenbergii*. (A) X-ray computer tomography of the mandible (volume rendering reconstruction). Gray-scale images were pseudo-colored according to an RGB palette, with low mineral density in red and high density in blue. Note the higher density of the incisors (i) and the molars (m) compared to the basal segment (bs) and the rest of the cuticle (c). (B) CT image of the incisor, pseudo-colored as in (a), showing a sharp gradient of mineral/atomic-density, from the lightly mineralized basal segment to the triple dentition of the massive incisors. (C) Back-scattered SEM image of a longitudinal section of an incisor showing a high-density axis below the tooth point (red arrow). (D) Raman map of a longitudinal section of an incisor in which the normalized integrated intensities (I/I_{max}) of the phosphate peak at $950\text{--}965\text{ cm}^{-1}$ (blue) and the carbonate peak at $1065\text{--}1085\text{ cm}^{-1}$ (green) are represented in color coding. The epoxy resin used to embed the sample is shown in red. (E) Higher resolution Raman map of a longitudinal section of the incisor edge showing the intensity (I/I_{max}) distribution of the phosphate band ν_1 at 960 cm^{-1} in the tooth. (F) Raman intensity (I/I_{max}) map of the carbonate band ν_1 at 1080 cm^{-1} showing the relative increase in the amount of carbonate towards the tooth margins. (G) Raman intensity map (I/I_{max}) of the CH_3 band at 1380 cm^{-1} showing a sharp decrease in the amount of organic matter in the central line. (H) Raman map representing the position of the phosphate ν_1 band. A color-coded scale bar for the peak positions is shown in the inset (range: $952\text{--}962\text{ cm}^{-1}$).

points along the profile line are in constant distance. When a correlation between mechanical properties and composition was examined (Fig. 5A Fig. S4), the chemical analysis profiles were taken after the indentation test and were located parallel to the indentation line, shifted by a few microns to avoid topographic disruption caused by the indentations.

2.8. HRTEM/STEM/SAED

Focused ion beam (FIB) milling was used for the preparation of an electron transparent ultrathin lamella. TEM lamellae, milled from a polished section were prepared with a FEI Helios Dual Beam FIB (FEI, Hillsboro, OR, USA) with a thickness of $\sim 100\text{ nm}$. HRTEM, SAED and analytical TEM investigations, including EDS analysis in the scanning TEM (STEM) mode, were carried out using a JEOL JEM-2100F instrument operating at 200 kV . Selected area electron diffraction (SAED) patterns were obtained by positioning the selected area diffraction aperture of the TEM over the desired area of the film. Gatan DigitalMicrograph 3 software was used for FFT analysis of HRTEM lattice images. Schematic illustrations of the orientation relation models were obtained using CaRine Crystallography software.

2.9. Nanoindentation

Nanoindentation samples were polished prior the experiments. Their surface roughness was analyzed by SEM and measured to be less than 100 nm . Nanoindentation experiments were conducted using a Hysitron TI 950 TriboIndenter. A Berkovich diamond probe tip was used for the experiments. The experiments included a loading stage (linear ramp, 60 s) to a maximal load of 5 mN , which was kept steady for a certain time to exclude creep effects (60 s), followed by unloading (linear ramp, 60 s). The typical indentation depth was 450 nm . A minimal distance of $5\mu\text{m}$ was maintained between adjacent indentations to prevent coupling effects.

2.10. TGA-FTIR

Analyses were performed with a Q500-TA apparatus coupled to a Ni10X FTIR microscope (Thermo). About 20 mg of incisor tooth powder were loaded into and weighed in an Al crucible. Measurements were performed in the temperature range $25\text{--}1000\text{ }^\circ\text{C}$ at a constant heating rate of $10\text{ }^\circ\text{C}/\text{min}$ under nitrogen atmosphere ($90\text{ ml}/\text{min}$). Infrared spectra were recorded periodically during the entire run in the $4000\text{--}400\text{ cm}^{-1}$ range, at 8 cm^{-1} spectral resolution.

2.11. Finite-element analysis

Commercial finite-element software (ABAQUS/implicit 6.16) was used for the numerical simulation. The geometric model was constructed based on SEM images of the incisor. The incisor material was modeled as a linear elastic isotropic material that was realized via a 2-D, 3-node, linear plane stress triangle (CPS3 in ABAQUS element library). Young's modulus across the incisor finite-element model was modeled on the basis of the nanoindentation results. In the modeling, the base of the incisor was fixed, and uniform pressure was applied at the tip area.

2.12. Statistical analysis

Quantitative data were expressed as mean \pm SD. Statistical analysis was performed with one-way analysis of variance (ANOVA) using computer software (Origin 8.0, Originlab Corp. Northampton, MA). $P < 0.05$ was defined as a statistically significant difference

3. Results and discussion

3.1. Tooth characterization

A range of techniques were used to characterize the *M. rosenbergii* mandible, particularly the incisors. X-ray computer tomography images showed that the mineral density of the mandible was much higher than that of the rest of the head (Fig. 1A, SI Video 1). Within the incisor there was a significant mineral density gradient, from the heavily mineralized distal edge to the less mineralized basal segment (Fig. 1B). The density gradients at the incisors probably indicate the existence of a mechanically graded structure, as was shown in other crustaceans. Backscattered electron (BSE) microscopy of longitudinal sections of the incisor (Fig. 1C) showed that below the sharp edges, along an internal axis running from the distal edge to the base of the tooth (arrow), there was a prominent increase in BSE emission, indicating a higher mean atomic number (Z-contrast). Raman spectroscopic imaging of longitudinal sections of the incisor (Fig. 1D-H) elucidated the spatial distribution of the minerals and the organic matrix (SI Fig. S1). The Raman intensity map of phosphate (blue) and carbonate (green) (Fig. 1D) showed that the incisor edge is composed mainly of calcium phosphate in the form of ACP/apatite, and that the phosphatic sharp cusp is anchored in the basal segment composed mainly of ACC. Higher spatial-resolution Raman mapping confirmed that the phosphatic phase dominated most of the incisor (Fig. 1E-F). Evaluation of the organic matrix distribution (Raman intensity at 1380 cm^{-1} , attributed to symmetric CH_3 deformation, which is prominent in chitin [7]) showed a clear decrease in the content of the organic matrix in the area of the central axis (Fig. 1G). The relative distributions of ACP and apatite were estimated from the position of the phosphate peak (ν_1), which ranged from 952 cm^{-1} for ACP to $>960\text{ cm}^{-1}$ for crystalline apatite [8]. Maps of the phosphate peak position (Fig. 1H, Fig. S1C) showed a shift from ACP to crystalline apatite, as a major phase, towards the central axis of the incisor.

3.2. Chemical characterization of the central axis

Chemical analysis of longitudinal sections of the incisor by wavelength dispersive spectroscopy (WDS) and energy dispersive spectroscopy (EDS) showed the tooth to be comprised mainly of calcium phosphate but to be highly enriched with Zn, especially along the central axis (Fig. 2A-D). The increase in Zn correlated with an increase in atomic density (BSE) and a decrease in Ca

(Fig. 2B). The degree of Zn incorporation in the area of the central axis was not homogeneous, ranging from 22% to 57% of cations $[\text{Zn}/(\text{Zn} + \text{Ca})]$, at%, Table S1]. EDS profiles perpendicular to the central axis demonstrated that the Zn cation fraction increased gradually towards the central axis (Fig. 2C) and that the increase in the amount of zinc always correlated with a concomitant decrease in the amount of calcium, while the phosphorous remained nearly constant (Fig. 2D). These results suggest that zinc and calcium cations are exchangeable within the mineral. Estimation of the major components of the tooth by thermogravimetric analysis coupled with Fourier transform infrared analysis (TGA-FTIR) indicated that the tooth was comprised of calcium phosphate (56wt%), calcium carbonate (16wt%), organic matrix (11wt%) and water (17wt%), most of which was probably structural water contained within the ACP-ACC minerals (Fig. 2E, Fig. S2).

2.3. Crystallographic characterization

Powder X-ray diffraction of the incisor tooth showed broad peaks at $\sim 20^\circ$ and $\sim 30^\circ$ (2θ), which correspond to chitin and ACP [9], respectively (Fig. 3A, blue). Upon heating the incisor powder to 400°C , crystallization of calcite (probably from ACC) was observed, while the chitin signal vanished (Fig. 3A, green). At 500°C , the ACP crystallized to hydroxyapatite (Fig. 3A, red). We did not observe any zinc phosphate mineral phases (e.g., hopeite and scholzite), suggesting that the zinc was probably incorporated into the mineral structure of ACP or crystalline apatite. In-situ synchrotron micro-beam X-ray diffraction experiments on thin polished sections of the incisor cusp showed that the majority of the tooth was composed of ACP together with highly crystalline and oriented chitin (Fig. 3B). Importantly, along the high-Zn central axis, the intensity of the chitin phase decreased, and a diffraction pattern corresponding to crystalline apatite was observed (Fig. 3C and D). The diffraction patterns showed the c-axis of the apatite crystals to be preferentially oriented towards the tooth apex (green line in Fig. 3C) perpendicular to the impact surface. Interestingly, the c-axis of chitin [(002) (013)] was oriented almost collinearly with the apatite c-axis, as has also been reported in crayfish teeth [2]. The c-axis of chitin (which corresponds to the longitudinal axis of the polymer chains and the nanofibrils) is the stiffest direction of the lattice [10], as is also assumed for the c-axis of apatite [11]. In the apatite diffraction pattern, the peak corresponding to the a-axis (300) was shifted to higher angles (lower d-spacings), while the peak corresponding to the c-axis (002) remained unchanged in comparison to the hydroxyapatite standard (PDF No: 9-432). This observation suggests that the a-axis of the Zn-apatite is contracted, whereas the c-axis seemed to be unaffected. The increase in the crystallinity of the calcium phosphate phase from the periphery of the incisor to the center together with the concomitant decrease in the amount of chitin is in agreement with the results of the Raman mapping (Fig. 1G and H).

3.4. High resolution transmission electron microscopy (HRTEM)

An ultra-thin section of the high-Zn zone, was prepared by focused ion beam (FIB) milling, and observed by HRTEM. The images showed chitin-protein nanofibrils (Fig. 4A), but no crystalline phase. EDS analyses (Fig. S3, Table S2) confirmed the composition of high-zinc calcium phosphate with an average substitution level $[\text{Zn}/(\text{Zn} + \text{Ca})]$ of 38%. Electron diffraction measurements performed on the tooth showed only diffuse powder rings consistent with the presence of an amorphous phase (Fig. 4B). Since the Raman spectra (Fig. 1H) and synchrotron micro-beam XRD (Fig. 3C-D) strongly suggest a dominant crystalline apatite phase at the central axis, we assume that the absence of apatite signal at the SAED is due to FIB "amorphous damage". The preparation of the sample for HRTEM by

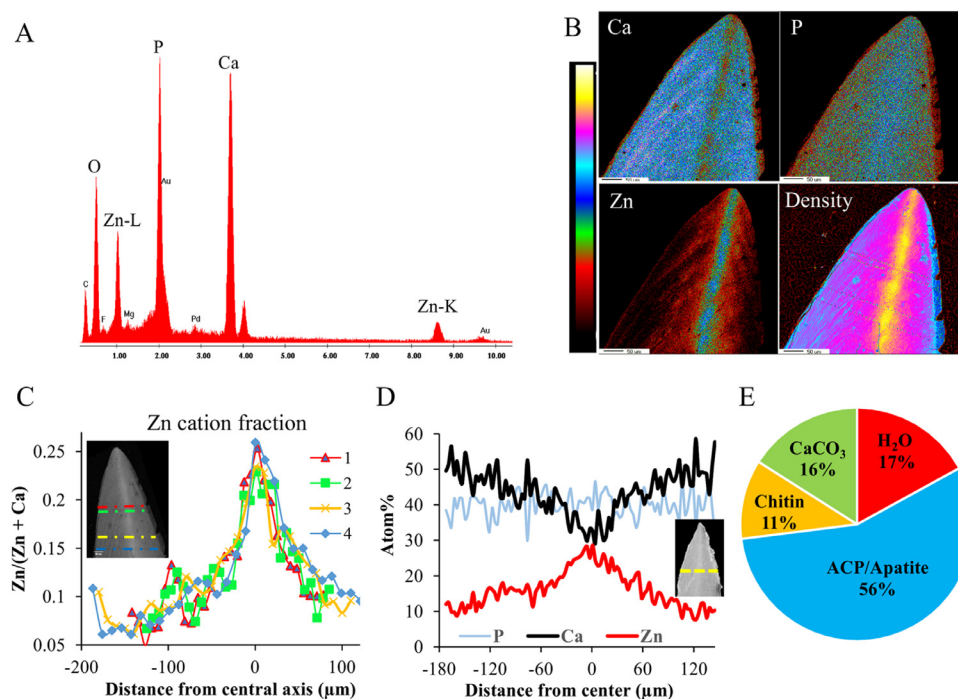


Fig. 2. Chemical characterization of an incisor tooth. (A) Typical EDS spectrum for the high-zinc zone. The major constituent elements are (calculated mass fraction): O (32%), Ca (20%), Zn (10%), P (14%) and F (2%). C was also detected, but its quantification (21%) is less reliable. (B) WDS mapping of a longitudinal section showing, qualitatively, the abundance of Ca, P, and Zn, and the corresponding atomic density. The internal axis of the incisor is enriched with Zn, depleted in calcium, and slightly enriched with phosphorous. (C) Analysis of four EDS profiles, perpendicular to the long axis of the tooth, of a polished longitudinal section ($N = 120$ points) showing the gradual increase of the Zn cation fraction ($Zn/(Zn + Ca)$ atom%) from 5–10% along the margins to 23–26% along the central axis (average = $12 \pm 5SD$). (D) Plot of the relative proportions of Ca, Zn and P (atom%) obtained from an EDS line profile (300 μm , 100 points) perpendicular to the long axis of the tooth (from different animal), demonstrating the complementary change of Ca and Zn, while the relative proportion of P remains quite steady. In this tooth, the Zn cation fraction ($Zn/Zn+Ca$) along the central axis (width = 40 μm , $N = 17$) was 40% ($\pm 5\%$ SD). (E) Estimated composition of the major components of the incisor tooth based on TGA-FTIR analyses (Fig. S2); ACP/apatite (56 wt%), water (17 wt%), ACC (16 wt%) and organic matter (11 wt%).

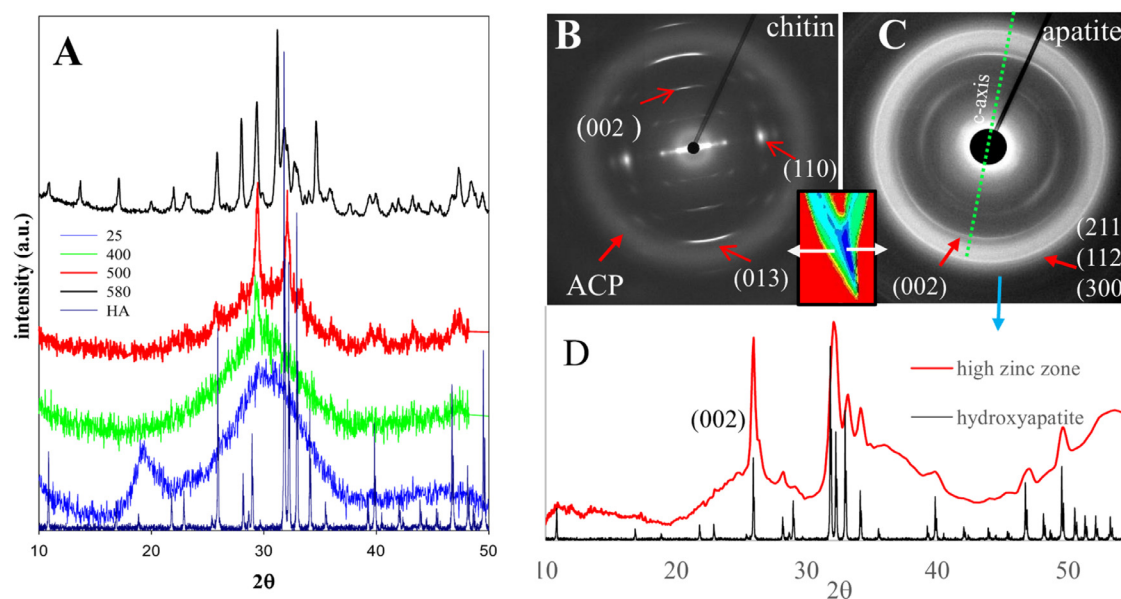


Fig. 3. crystallographic properties of the incisor. (A) Powder XRD of the incisor (50 teeth). Blue; powder XRD of untreated powdered tooth, exhibiting a diffraction peak at $2\theta = 19.2^\circ$, attributed to the (110) lattice plane of chitin, and at $2\theta \approx 31^\circ$, attributed to a convolution of the (112), (211) and (300) lattice planes of poorly crystalline HA and ACP. Green; powder XRD obtained after heating to 400 $^\circ C$; a peak at $2\theta = 29.4^\circ$, assigned to lattice plane (104) of calcite, is evident. Red; powder XRD obtained after heating to 500 $^\circ C$; in addition to the calcite peak, a new peak at $2\theta = 32.1$ indicates that part of the ACP crystallized to hydroxyapatite (lattice plane (211,112)). (B) Diffraction pattern of the periphery of a longitudinal section of the incisor tooth obtained using synchrotron microbeam X-ray radiation. The pattern is comprised of a highly oriented and crystalline chitin phase [with peaks at d-spacings of 3.39, 4.6 and 5.17 \AA corresponding to the (013), (110) and (002) lattice planes, respectively] together with diffuse powder rings originating from ACP. (C) Diffraction pattern of the high-zinc central zone showing a crystalline apatite pattern with peaks corresponding to lattice plane (002) at 3.43 \AA , and to lattice planes (211), (112), (300) at ~ 2.8 \AA . The apatite crystals are preferentially oriented along the c-axis (002) (green line), pointing towards the tooth apex. (D) Integrated diffraction pattern obtained following subtraction of most of the chitin phase reveals the presence of highly crystalline apatite along the high-zinc central axis. The identified lattice planes are 3.42 \AA (002), 2.8 \AA (211), 2.7 \AA (300), 2.625 \AA (202), 1.93 \AA (222) and 1.836 \AA (213).

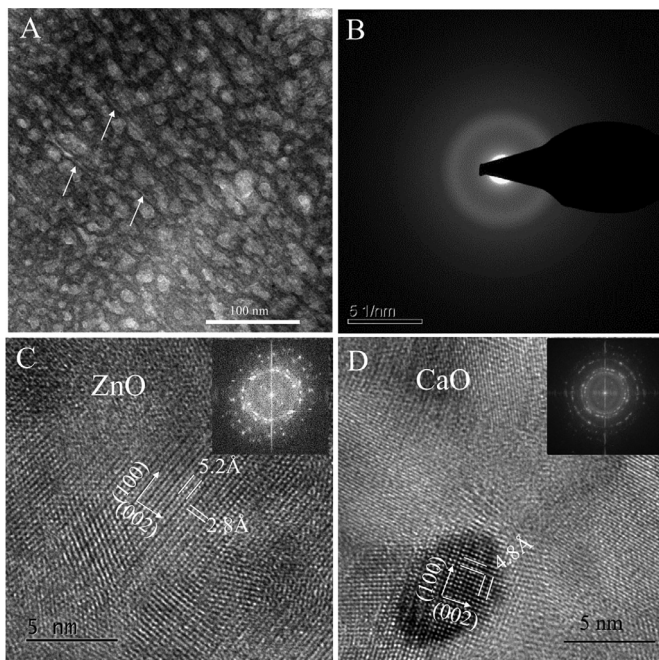


Fig. 4. HRTEM images of the high-Zn zone. (A) Chitin nanofibrils, about 3 nm in diameter, oriented perpendicular to the tooth edge. These nanofibrils represent the basic chitin unit of 18–25 polysaccharide molecular chains in the form of narrow and long crystalline units. (B) Selected area electron diffraction (SAED) showing the diffuse powder ring characteristic of ACP. It is possible that this amorphous phase is result of the FIB milling which is known to induces amorphous damage [12]. Under the electron beam, the amorphous material crystallized, and two minerals were identified—hexagonal zinc-oxide (C) and cubic calcium-oxide (D). Inset: FFT of the respective zones.

focused ion beam (FIB) lift-out technique, entail rather aggressive milling process. The bombardment by highly accelerated gallium ion beams might produce some damages and artifacts. One of the known artifacts is the “amorphous damage” in which the ion beam amorphizes the outer layer of the specimen [12]. Upon further exposure to the electron beam, the amorphous material started to crystallize, but not to apatite. Rather, two minerals were identified according to the HRTEM images and FFT; zinc oxide (Fig. 4C) and calcium oxide (Fig. 4D). The phenomenon of ACP crystallization to CaO and not to apatite, under high electron beam current, was reported before [13]. To conclude, although we couldn’t characterize the high-zinc apatite by HRTEM, the crystallization to ZnO and CaO confirm that the zinc is part of the mineral phase and not part of the organic material as is the common case in invertebrates.

3.5. Mechanical properties

To examine the possible functionality of the high-Zn axis, we performed nanoindentation measurements along line profiles perpendicular to the tooth axis. The results showed a significant increase in elastic modulus and hardness from the margins towards the central axis, which was clearly associated with the increased Zn/Ca ratio (Fig. 5A, Fig. S4A–H). Compilation of the results from four profiles ($N = 93$) showed that the increase in Zn/Ca ratio correlated well with the increased modulus (Fig. 5B).

On the structural level, the high-Zn zone forms an internal rigid element, positioned beneath the serrated tooth ridge which is exposed to maximal load stress during biting. Finite-element simulations of biting forces (Fig. 5C, Fig. S5), indicated that the high-Zn axis constituted a high-modulus path through which stress is directed along the tooth from the sharp tips to the more pliable tooth base. This probably promotes energy absorption and damage

resilience via the ductility and viscoelasticity of the bio-composite [2,3,14–16]. This internal rigid element possibly represents a unique bio-chemical-mechanical strategy for stress transfer. This strategy which is very common in building constructions, is markedly different from the widespread bio-mechanical principles in invertebrate and vertebrate teeth, in which the stress is transmitted from the crown to the root through a bulk material, such as dentin.

3.6. Zinc incorporation mode

Zinc reinforcement of the mandibles of insects, scorpions and polychaetes has previously been reported, but in those studies, zinc was thought to be part of the organic matrix [17–21]. In contrast, our results strongly suggest that the zinc is part of the mineral phase. The observations that an increase in the amount of zinc always correlated with a decrease in the amount of calcium (Fig. 2B, D), the decrease in apatite lattice parameters (Fig. 3D), and the formation of ZnO under electron beam irradiation (Fig. 4C), strongly suggest that Zn substitutes Ca within the mineral phase. Furthermore, mass balance calculations (Fig. S2), suggest that in the high-Zn zone, the amount of Zn exceeds the total amount of organic matter, thereby excluding the option that Zn is part of the proteinaceous matter as a cross-linking agent.

The incorporation of zinc into inorganic apatite, is an example of the more general phenomenon of ionic substitutions in apatite. The subject of ionic substitution was widely studied in natural and synthetic apatite, due to the importance of the mineral in biomedical applications and the remarkable tolerance of the apatite structure that can accommodate varied ionic substitutions without a significant change in its symmetry [22–24]. Zn-substituted apatite was also considerably studied [22,25–28], usually in the context of synthetic materials, because biogenic Zn-substituted apatite, (excluding zinc as a trace element [29]) has not been documented yet.

The exact mode of Zn incorporation into hydroxyapatite is not agreed upon [25–27,30,31]. It was suggested that Zn^{2+} ions can replace Ca^{2+} ions in the apatite structure and that a Ca(II) site at the boundaries of the hydroxyl channel would be energetically favored over a Ca(I) site [26]. Since the ionic radius of Zn^{2+} (0.74 Å) is considerably smaller than that of Ca^{2+} (0.99 Å), Zn substitution will inhibit the synthesis of hydroxyapatite and reduce its crystallinity [32]. Previous descriptions of synthetic zinc-substituted hydroxyapatite ceramics indicate that the highest possible level of Zn incorporation into hydroxyapatite is 15–20%; at higher levels, the mineral becomes amorphous [22]. However, our results suggest that the Zn substitution level in the bioapatite can exceed 50% and that it is, surprisingly, associated with increased crystallinity. This apparent anomaly probably indicates that the biologically controlled Zn incorporation might involve biomolecules that stabilize the strained lattice, as was suggested for other biominerals [33].

3.7. Possible explanations for the zinc reinforcement effect

The way in which Zn substitution improves the stiffness and hardness of apatite (and ACP) is not as yet clear. Synthetic Zn-substituted hydroxyapatite was found to be an efficient material for biomedical applications [23–25,34], but usually the reported advantages do not include mechanical enhancement. The few reports on the effect of Zn substitution on mechanical properties of apatite [35,36] relate to low substitution levels ($\leq 2\%$) and don’t show a significant effect of zinc substitution on the mechanical properties. Some of the experiments show a small decrease in microhardness and fracture toughness [35] while other experiments show a small increase in hardness [36].

The stiffness of most materials depends on two factors: bond stiffness and the density of bonds per unit volume [37]. Zn sub-

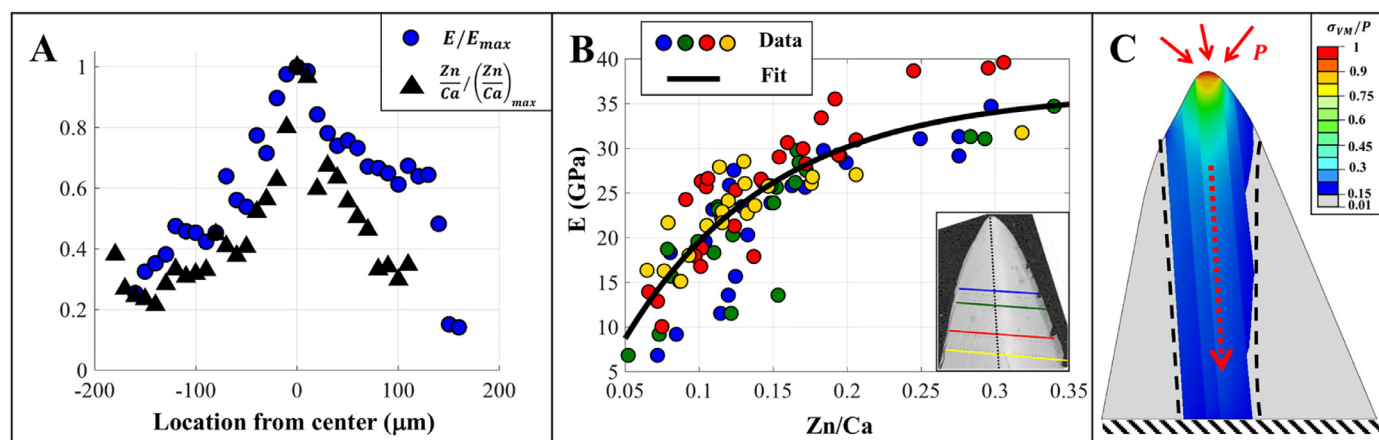


Fig. 5. Correlation between the mechanical characteristics of the incisor and the Zn/Ca ratio (calculated from the same dataset of Fig. 2C). (A) Representative Zn/Ca ratios (black triangles) and Young's modulus values (blue circles), E (GPa), normalized to their maximal values, shown at different locations from the incisor's center. Both Zn/Ca and E are maximal along the incisor center, with values being about three times higher than at the tooth periphery. (B) Compilation of all nanoindentation results (four profiles, $N = 93$) and their corresponding Zn/Ca ratios (blue, green, red and yellow circles) shows a clear positive correlation between E and the Zn/Ca ratio and follows an exponential trend (black line) expressed as $E(\text{Zn/Ca} = x) = (E_{\infty} - E_0) \cdot [1 - \exp(-(x - x_0)/k)] + E_0$. The fitting coefficients are $E_0 = 8.7 \text{ GPa}$ and $E_{\infty} = 36.8 \text{ GPa}$, which represent the initial ($x_0 = \text{Zn/Ca} = 0.05$) and asymptotic bounds for E , and $k = 0.1$ which represents the scale of the substitution effect. Insert: SEM micrograph of the analyzed zones (color coded) showing the corresponding indentation profiles. (C) Finite-element analysis that models a biting event by introducing pressure (P) to the incisor tip (red arrows); the incisor base is kept fixed. The resultant von Mises stress distribution is normalized to the applied pressure (σ_{VM}/P). The incisor experiences high stress at the near-tip region with the high Zn/Ca ratio. The stress transmission path from the incisor tip to the basal segment (red dashed arrow) is conducted mostly through the high-zinc region (indicated by the black dashed lines).

stitutes are assumed to form Zn–O bonds that are shorter and more covalent in character than those of Ca–O [38], which is usually an indication of stiffer bonds. A well-known material engineering concept, “solid solution strengthening” might also be relevant. In this strategy, the mechanical properties of materials are enhanced by the incorporation of foreign ions (interstitial and/or substitutional) with different ionic radii, which cause lattice distortions that hinder dislocation motion, thereby increasing the yield stress of the material. Indeed, several studies of high-magnesium calcite in echinoderms suggest a similar strengthening mechanism in biominerals as well [39–41].

Mineral-organic interface: The quality of the mineral-organic interface was shown to be a crucial factor in determining the overall strength of a composite material [42,43]. Although the nanoindentation tests we made are less efficient in characterizing such bulk properties, it is possible that zinc with its well-known protein bonding capabilities [44,45], plays a role in strengthening mineral-organic interface and increases the overall strength of the incisor structure. However, assuming a substitutional context, i.e. that zinc is located at the cation sites of apatite (Ca[I] or Ca[II]) and that the substitution must fulfill an overall charge balance in the mineral, the coordination environment of zinc does not favor ligand bindings or other foreign interfacial affairs. Thus, such a function, if exists, cannot explain the high zinc (and low calcium) at the central axis. Yet, it is possible that part of the zinc ions, maybe at the outer boundaries of the crystals, play a role in the reinforcement of the mineral-organic interface.

4. Conclusions

The mandible of *M. rosenbergii* demonstrates an elaborate structure in which biomechanical features are controlled by fine tuning of several parameters, such as, crystallinity degree, mineral density, mineral composition (calcium carbonate vs calcium phosphate), and orientational alignment. Most interestingly, the incisor's cusps which seem to be the most mechanically challenged site, are highly enriched by zinc. Various analytical methods, including microbeam XRD, high resolution TEM and electron diffraction, suggest that the zinc is part of the mineral phase where it

substitutes calcium ions in the bioapatite. A clear correlation between the Zn substitution level and stiffness and hardness, suggests that the substitution serves for mechanical reinforcement of the tooth bioapatite. On one hand zinc hinders apatite crystallization, but on the other hand it is possible that thanks to these same distortional properties, incorporated Zn can enhance the mechanical feature of apatite by impeding dislocations propagation in the distorted crystal lattice, as applied in “solid solution strengthening”. Perhaps, by introducing biomolecules that can alleviate Zn-apatite crystal strain, the biomineralization mechanism can resolve these contradictory effects of Zn. Thus, potential biomimetic applications, requires the identification and characterization of the organic matrix molecule involved in the process. The Zn-rich mineral, which shows enhanced mechanical properties, forms an internal structure that probably serves as a load transfer element, directing stress from the biting cusps to the underlying compliant layers. It is generally held that in biological structures, mechanical features like stiffness and toughness gradients are achieved largely through the arrangement of the structural components at many hierarchical levels rather than through manipulation of the chemical composition [46,47]. Our study suggests that crustaceans have recruited chemistry to complement hierarchical structure. We submit that this innovative mineralogy has the potential for application in the development of improved biomaterials, e.g., synthetic calcium phosphate derivatives for human bone and tooth grafts.

Declaration of Competing Interest

The authors declare that they have no known competing financial interests or personal relationships that could have appeared to influence the work reported in this paper.

Acknowledgments

We thank the Dor Aquaculture Research Station of the Israel Ministry of Agriculture and Rural Development for animal supply. We thank Hazel Garvey-Cook (Renishaw plc) for the help in Raman mapping and Dr. Vladimir Ezersky for his help in XRD FFT. We thank Prof. M. Edelman for critically reading the manuscript

and his valuable assistance. This research was partly supported by the [Israel Science Foundation](#) (grant No. 354/18) and the National Institute for Biotechnology in the Negev (NIBN).

Supplementary materials

Supplementary material associated with this article can be found, in the online version, at [doi:10.1016/j.actbio.2020.07.039](https://doi.org/10.1016/j.actbio.2020.07.039).

References

- [1] J.F.V. Vincent, Arthropod cuticle: a natural composite shell system, *Composites Part A-Applied Science and Manufacturing* 33 (10) (2002) 1311–1315.
- [2] S. Bentov, P. Zaslansky, A. Al-Sawalmih, A. Masic, P. Fratzl, A. Sagi, A. Berman, B. Aichmayer, Enamel-like apatite crown covering amorphous mineral in a crayfish mandible, *Nat Commun* 3 (2012) 839.
- [3] S. Bentov, E.D. Aflalo, J. Tynyakov, L. Glazer, A. Sagi, Calcium phosphate mineralization is widely applied in crustacean mandibles, *Sci Rep-Uk, Macmillan Publishers Limited* (2016) 22118.
- [4] S. Bentov, S. Abehsera, A. Sagi, The mineralized exoskeletons of crustaceans, in: E. Cohen, B. Moussian (Eds.), *Extracellular Composite Matrices in Arthropods*, Springer, New York, 2017.
- [5] Y. Pan, M.E. Fleet, Compositions of the apatite-group minerals: substitution mechanisms and controlling factors, *Reviews in Mineralogy and Geochemistry* 48 (1) (2002) 13–49.
- [6] S.J. Omelon, M.D. Grynopas, Relationships between polyphosphate chemistry, biochemistry and apatite biomineralization, *Chem. Rev.* 108 (11) (2008) 4694–4715.
- [7] D. Lin-Vien, N.B. Colthup, W.G. Fateley, J.G. Grasselli, *The Handbook of Infrared and Raman Characteristic Frequencies of Organic Molecules*, Elsevier, 1991.
- [8] G. Sauer, W. Zunic, J. Durig, R. Wuthier, Fourier transform Raman spectroscopy of synthetic and biological calcium phosphates, *Calcif. Tissue Int.* 54 (5) (1994) 414–420.
- [9] A.S. Posner, F. Betts, Synthetic Amorphous Calcium-Phosphate and Its Relation to Bone-Mineral Structure, *Accounts Chem Res* 8 (8) (1975) 273–281.
- [10] A. Al-Sawalmih, C. Li, S. Siegel, H. Fabritius, S. Yi, D. Raabe, P. Fratzl, O. Paris, Microtexture and chitin/calcite orientation relationship in the mineralized exoskeleton of the American lobster, *Adv Funct Mater* 18 (20) (2008) 3307–3314.
- [11] B. Viswanath, R. Raghavan, U. Ramamurthy, N. Ravishankar, Mechanical properties and anisotropy in hydroxyapatite single crystals, *Scr Mater* 57 (4) (2007) 361–364.
- [12] L.A. Giannuzzi, F.A. Stevie, A review of focused ion beam milling techniques for TEM specimen preparation, *Micron* 30 (3) (1999) 197–204.
- [13] A. Meldrum, L. Wang, R. Ewing, Electron-irradiation-induced phase segregation in crystalline and amorphous apatite: a TEM study, *American Mineralogist* 82 (9–10) (1997) 858–869.
- [14] B. Bar-On, F.G. Barth, P. Fratzl, Y. Politi, Multiscale structural gradients enhance the biomechanical functionality of the spider fang, *Nat Commun* 5 (2014) 3894.
- [15] I. Kellersztein, S.R. Cohen, B. Bar-On, H.D. Wagner, The exoskeleton of scorpions' pincers: structure and micro-mechanical properties, *Acta Biomater* 94 (2019) 565–573.
- [16] B. Bar-On, On the form and bio-mechanics of venom-injection elements, *Acta Biomater* 85 (2019) 263–271.
- [17] H.C. Lichtenegger, T. Schoberl, J.T. Ruokolainen, J.O. Cross, S.M. Heald, H. Birkedal, J.H. Waite, G.D. Stucky, Zinc and mechanical prowess in the jaws of Nereis, a marine worm, *Proc. Natl. Acad. Sci. U.S.A.* 100 (16) (2003) 9144–9149.
- [18] Y. Politi, M. Prieuwasser, E. Pippel, P. Zaslansky, J. Hartmann, S. Siegel, C. Li, F.G. Barth, P. Fratzl, A spider's fang: how to design an injection needle using chitin-based composite material, *Adv Funct Mater* 22 (12) (2012) 2519–2528.
- [19] R.M.S. Schofield, M.H. Nesson, K.A. Richardson, Tooth hardness increases with zinc-content in mandibles of young adult leaf-cutter ants, *Naturwissenschaften* 89 (12) (2002) 579–583.
- [20] R. Schofield, M. Nesson, K.A. Richardson, P. Wyeth, Zinc is incorporated into cuticular "tools" after ecdysis: the time course of the zinc distribution in "tools" and whole bodies of an ant and a scorpion, *J. Insect Physiol.* 49 (1) (2003) 31–44.
- [21] C.C. Broomell, M.A. Mattoni, F.W. Zok, J.H. Waite, Critical role of zinc in hardening of Nereis jaws, *J Exp Biol* 209 (16) (2006) 3219–3225.
- [22] A. Bigi, E. Boanini, M. Gazzano, Ion substitution in biological and synthetic apatites, in: C. Aparicio, M.-P. Ginebra (Eds.), *Biomineralization and Biomaterials*, Woodhead Publishing, Boston, 2015, pp. 235–266.
- [23] M. Šupová, Substituted hydroxyapatites for biomedical applications: a review, *Ceram Int* 41 (8) (2015) 9203–9231.
- [24] J.H. Shepherd, D.V. Shepherd, S.M. Best, Substituted hydroxyapatites for bone repair, *Journal of Materials Science: Materials in Medicine* 23 (10) (2012) 2335–2347.
- [25] E. Thian, T. Konishi, Y. Kawanobe, P. Lim, C. Choong, B. Ho, M. Aizawa, Zinc-substituted hydroxyapatite, a biomaterial with enhanced bioactivity and antibacterial properties, *Journal of Materials Science: Materials in Medicine* 24 (2) (2013) 437–445.
- [26] Y. Tang, H.F. Chappell, M.T. Dove, R.J. Reeder, Y.J. Lee, Zinc incorporation into hydroxylapatite, *Biomaterials* 30 (15) (2009) 2864–2872.
- [27] F. Miyaji, Y. Kono, Y. Suyama, Formation and structure of zinc-substituted calcium hydroxyapatite, *Mater Res Bull* 40 (2) (2005) 209–220.
- [28] R.Z. LeGeros, C.B. Bleiwas, M. Retino, R. Rohanizadeh, J.P. LeGeros, Zinc effect on the in vitro formation of calcium phosphates: relevance to clinical inhibition of calculus formation, *Am J Dent* 12 (2) (1999) 65–71.
- [29] J. Aitken, Factors affecting the distribution of zinc in the human skeleton, *Calcif Tissue Res* 20 (1) (1976) 23–30.
- [30] F. Ren, R. Xin, X. Ge, Y. Leng, Characterization and structural analysis of zinc-substituted hydroxyapatites, *Acta Biomater* 5 (8) (2009) 3141–3149.
- [31] E. Boanini, M. Gazzano, A. Bigi, Ionic substitutions in calcium phosphates synthesized at low temperature, *Acta Biomater* 6 (6) (2010) 1882–1894.
- [32] R. LeGeros, M. Taheri, G. Quiroigco, J. LeGeros, Formation and stability of apatites: effects of some cationic substituents, in: *Proc 2nd International Congress on Phosphorus Compounds*, Boston, 1980, pp. 89–103.
- [33] B. Pokroy, J.P. Quintana, N.C. El'ad, A. Berner, E. Zolotoyabko, Anisotropic lattice distortions in biogenic aragonite, *Nat Mater* 3 (12) (2004) 900–902.
- [34] T.J. Webster, E.A. Massa-Schlueter, J.L. Smith, E.B. Slamovich, Osteoblast response to hydroxyapatite doped with divalent and trivalent cations, *Biomaterials* 25 (11) (2004) 2111–2121.
- [35] I. Uysal, F. Severcan, Z. Evis, Structural and mechanical characteristics of nanohydroxyapatite doped with zinc and chloride, *Advances in Applied Ceramics* 112 (3) (2013) 149–157.
- [36] S.J. Kalita, H.A. Bhatt, Nanocrystalline hydroxyapatite doped with magnesium and zinc: synthesis and characterization, *Materials Science and Engineering: C* 27 (4) (2007) 837–848.
- [37] M.F. Ashby, Materials selection in mechanical design, *Metallurgia Italiana* 86 (1994) 475–475.
- [38] X. Ma, D.E. Ellis, Initial stages of hydration and Zn substitution/occupation on hydroxyapatite (0 0 0 1) surfaces, *Biomaterials* 29 (3) (2008) 257–265.
- [39] R. Wang, L. Addadi, S. Weiner, Design strategies of sea urchin teeth: structure, composition and micromechanical relations to function, *Philosophical Transactions of the Royal Society of London B: Biological Sciences* 352 (1352) (1997) 469–480.
- [40] Y. Ma, S.R. Cohen, L. Addadi, S. Weiner, Sea Urchin Tooth Design, An "All-Calcite" Polycrystalline Reinforced Fiber Composite for Grinding Rocks, *Advanced Materials* 20 (8) (2008) 1555–1559.
- [41] M.E. Kunitake, S.P. Baker, L.A. Estroff, The effect of magnesium substitution on the hardness of synthetic and biogenic calcite, *MRS Commun* 2 (03) (2012) 113–116.
- [42] J.W. Dunlop, P. Fratzl, Biological composites, *Annu Rev Mater Res* 40 (2010) 1–24.
- [43] P. Gilbert, M. Abrecht, B.H. Frazer, The organic-mineral interface in biominerals, *Reviews in Mineralogy and Geochemistry* 59 (1) (2005) 157–185.
- [44] D.S. Auld, in: *Zinc Coordination Sphere in Biochemical Zinc sites*, *Zinc Biochemistry, Physiology, and Homeostasis*, Springer, 2001, pp. 85–127.
- [45] W. Maret, Y. Li, Coordination dynamics of zinc in proteins, *Chem. Rev.* 109 (10) (2009) 4682–4707.
- [46] P. Fratzl, R. Weinkamer, Nature's hierarchical materials, *Prog Mater Sci* 52 (8) (2007) 1263–1334.
- [47] J. Aizenberg, J.C. Weaver, M.S. Thanawala, V.C. Sundar, D.E. Morse, P. Fratzl, Skeleton of *Euplectella* sp.: structural hierarchy from the nanoscale to the macroscale, *Science* 309 (5732) (2005) 275–278.